Journal of Magnetism and Magnetic Materials 476 (2019) 589–596

Contents lists available at ScienceDirect

Journal of Magnetism and Magnetic Materials

journal homepage: www.elsevier.com/locate/jmmm

Research articles

Chaotic patterns and localized states in spin valves

Ana. M. Cabanas[a,*], Marcel G. Clerc[b], David Laroze[a], Alejandro O. Leon[c]

[a] Instituto de Alta Investigación, CEDENNA, Universidad de Tarapacá, Casilla 7D, Arica, Chile
[b] Departamento de Física and Millennium Institute for Research in Optics, Facultad de Ciencias Físicas y Matemáticas, Universidad de Chile, Casilla 4873, Santiago, Chile
[c] Instituto de Física, Pontificia Universidad Católica de Valparaíso, Casilla 4059, Chile

ARTICLE INFO

Keywords:
Nonlinear dynamic
Landau-Lifshitz-Gilbert-Slonczewski equation
Chaos

ABSTRACT

Driven nano-magnets have attracted increasing attention due to their potential applications and complex dynamical behavior. Spin valves are possibly the most studied driven nano-magnets because applied magnetic fields and electric currents can control their magnetization. Due to these properties, spin valves are proposed candidates for the new generation of memory units. Based on the Landau-Lifshitz-Gilbert-Slonczewski equation, we show that this system exhibits a wide range of magnetization textures, such as patterns, domain walls, and localized structures. Monitoring the Largest Lyapunov exponent, we demonstrate that these textures are chaotic. We numerically characterize the dynamical behavior of this device using the magnetic energy and the magnetoresistance. Finally, we present a phase diagram of the different types of spatial solutions as a function of the applied current and the field.

1. Introduction

When a macroscopic system is driven out of thermodynamic equilibrium, it exhibits spatially periodic states or patterns [1–3]. These textures usually emerge as the result of a *symmetry-breaking instability of a uniform state*. When the system is subjected to a more significant energy injection, stationary patterns can become unstable and give rise to more complex textures. For example, chaotic localized states arise from steady localized states when a control parameter is increased [4,5]. Furthermore, a usual hallmark of the spatially extended non-equilibrium system is spatiotemporal chaos, characterized by dynamics that are aperiodic in time and space with sensitive dependence on the initial conditions [6,7]. Understanding the origin of spatiotemporal order, the selection mechanisms of the spatial structures and the routes that lead to spatiotemporal chaos from stationary patterns are major themes of interest in nonlinear science.

Let us focus on the particular case of driven nano-magnets. Dissipative magnetization dynamics is a phenomenon that has gained renewed interest in the scientific community because of the applications in magnetic memory and current-induced magnetization devices [8–10]. Magnetic states can be created and controlled by applying external magnetic fields [11], pure electric voltages [12], pure spin-currents [13] and spin-polarized electric currents. The last mechanism is based on the *spin-transfer-torque* (STT) effect predicted by Slonczewski [14,15] and Berger [16]. The STT consist of the transfer of spin-angular momentum from electric currents to the localized spins of the magnetic material [17–19].

The Landau-Lifshitz-Gilbert-Slonczewski equation is the continuous description for driven nano-magnets [15]. It accounts for the general case of magnetization interacting with both spin-polarized currents and magnetic fields. This equation can be transformed into the well-known generalized Nonlinear Schrödinger equation [20], which describes nonlinear dissipative waves [21]. Then, the dynamics of driven magnets have several similarities and share some behavior with other physical systems outside of equilibrium [21–24].

In our case, by varying the electric current and the applied field the system exhibit bistability between homogeneous states and patterns, which is one of the main ingredients to find localized states [2,25], known as *solitons* [26]. Solitonic modes have been experimentally observed in nano-oscillators [27–29]. State of the art for conservative and dissipative localized state can be found in Refs. [26,25,24]. In addition to conventional soliton, there are other localized states that exist in different types of systems [30–34,36,35,37].

In driven nano-magnets, complicated spatiotemporal magnetization structures emerge due to the combined effects of the spin-polarized current, spatial coupling and dissipation. As a consequence intricate dynamical behaviors and chaos [38–45] may appear.

The purpose of the present work is to characterize the existence of chaotic patterns, domain walls and localized structures in driven nano-magnets. The paper is organized as follows. After introducing the setup

* Corresponding author.
E-mail address: ana.cabanas.plana@gmail.com (A.M. Cabanas).

https://doi.org/10.1016/j.jmmm.2019.01.027
Received 30 August 2018; Received in revised form 16 December 2018; Accepted 7 January 2019

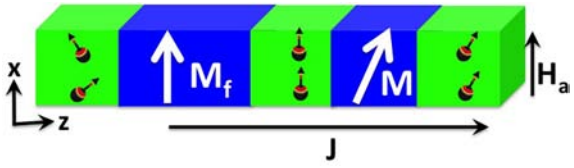

Fig. 1. Schematic representation of a spin-valve device, the light (green) and dark (blue) layers represent the nonmagnetic and the magnetic metal film, respectively. (For interpretation of the references to colour in this figure legend, the reader is referred to the web version of this article.)

device and the theoretical description, the dynamical indicators are presented in Section 2. The main numerical results and simulation details are described in Section 3. We numerically show that in a region of the parameter space the pattern solution coexists with a homogeneous one. In addition, we find a family of localized states that connect asymptotically a uniform state with a chaotic pattern. Furthermore, we study the dynamical evolution of the localized structures and the patterns through time series analysis, the largest Lyapunov exponent and the Fourier spectrum. Section 4 presents a summary and a phase diagram of the system.

2. Model

Spin-transfer torques are usually studied in spin valves, a pillar structure with nanometer-scale dimensions. A spin valve has at least two magnetic layers separated by a nonmagnetic material layer, the spacer. The lateral size is of order of 100 nm. The *fixed* layer, with magnetization $\mathbf{M_f}$, has a large magnetocrystalline anisotropy or is thicker than the free layer acting as a *polarizer* for the electric current as it is shown in Fig. 1. The magnetization of the thinner *free* layer, $\mathbf{M}$, can point in any direction. The control parameters are the external magnetic field $\mathbf{H_a}$ and the electric current J flowing through the spin valve.

We focus on the case in which both the polarizer and the magnetic field are collinear. When a spin-polarized current enters into a ferromagnet, the conduction electron spins interact with the local magnetization of the magnetic film [17]. This interaction produces a precession and reorientation of the electron spin on transmission through the ferromagnetic layer. Contributions arising from exchange, anisotropy, self-magnetostatic and applied field interactions are taken into account in the energy of the system that has the dimensionless form [46]

$$E = \int \left[\frac{1}{2}\left(\frac{\partial \mathbf{m}}{\partial x}\right)^2 - \mathbf{h_a}\cdot\mathbf{m} - \frac{\beta_x}{2}m_x^2 + \frac{\beta_z}{2}m_z^2 \right] dx, \tag{1}$$

where $\mathbf{m}$ is the unitary magnetization vector of the free layer in terms of its saturation magnetization M_s, $\mathbf{m}(x,t) \equiv \mathbf{M}/M_s$. We assume that the free magnetization layer is small enough in one of the lateral dimensions to guarantee that the magnetization depends on one of the spatial coordinates only, x. The dimensionless external magnetic field $\mathbf{h_a} \equiv \mathbf{H_a}/M_s = h_a\mathbf{e_x}$ points along the x-axis parallel to the magnetization of the fixed layer. The energy E is normalized by the shape anisotropy energy of the thin film $\mu_o M_s^2/2$, where $\mu_o = 4\pi \times 10^{-7}$ N/A^2 is the vacuum permeability. Typical experimental values for cobalt materials are $M_s(Co) \approx 1.42 \times 10^6$ A/m ≈ 17.8 kOe. The coefficients β_x and β_z are the dimensionless anisotropy constants for the x-axis (easy axis) and the z-axis (hard axis). They are account for the magnetocrystalline anisotropy and demagnetization effects. We assume that both coefficients are positive ($\beta_x = 1/2$ and $\beta_z = 1$) so β_x will favor the free magnetization in the x-axis while β_z will disfavor orientations along z-axis. It is worth mentioning that for thick cobalt layers, the magnetization equilibrium is in the sample plane [47,48]. On the other hand, subnanometer thick cobalt, the magnetization points perpendicular to the plane as a result of the interface anisotropy (see [49] and references therein). Thus, the perpendicular-to-plane anisotropy coefficient β_z can be controlled by the layer thickness. The distances are normalized with respect to the *exchange length*, $l_{ex} \equiv \sqrt{2a/(\mu_o M_s^2)}$. For instance, in a cobalt layer of 3 nm thickness, the effective exchange lattice constant for cobalt is $a \approx 1.5 \times 10^{-11}$ J/m and consequently $l_{ex}(Co) \approx 3.4$ nm.

The magnetization evolution of the free layer is described in the continuous limit by the Landau-Lifshitz-Gilbert-Slonczewski dimensionless equation [46,15,17]:

$$\frac{\partial \mathbf{m}}{\partial t} = -\mathbf{m}\times\mathbf{h}_{eff} + \alpha\mathbf{m}\times\frac{\partial \mathbf{m}}{\partial t} + g\,\mathbf{m}\times(\mathbf{m}\times\hat{\mathbf{p}}), \tag{2}$$

where $\mathbf{h}_{eff}$ is the effective field, α is the Gilbert damping constant, g is the spin-torque coefficient, and $\hat{\mathbf{p}} \equiv \mathbf{M_f}/|\mathbf{M_f}| = \mathbf{e_x}$ is the polarization vector of the current. The dimensionless time, written in terms of the modulus of the gyromagnetic constant, is $t = T|\gamma|M_s$ with $|\gamma| \approx 2.21 \times 10^5$ mA^{-1}s^{-1}. Therefore, in the case of cobalt, the characteristic time scale of our equation is $t_c = 1/|\gamma|\,M_s \approx 3.2$ ps. An important feature of this equation is the conservation of the modulus of magnetization $|\mathbf{m}|$ [20].

The first term on the right-hand side of Eq. (2) accounts for conservative precessions about the effective magnetic field. The effective field acting on the magnetization is the functional derivative of the energy E with respect to the magnetization [50] $\mathbf{h}_{eff} \equiv -\delta E/\delta\mathbf{m}$.

The second term of Eq. (2) is the phenomenological dissipation introduced by Gilbert [51] responsible for the relaxation of the magnetization to the equilibrium orientation. This relaxation phenomenon is quantified by α and depends on the geometry and the material of the spin-valve device. We assume that $\alpha = 0.05$ considering that typical experimental values are of 10^{-2} order [52,53].

The third term of Eq. (2) stands for the spin-transfer torque effect. The spin-polarized current will transfer angular momentum to the free layer. For electrons moving from the fixed to the free film ($J < 0$ and $g < 0$), the torque of the current has the same direction as the Gilbert damping and stationary behaviors are observed. For electrons flowing from the free to the fixed layer ($J > 0$ and $g > 0$), the spin-transfer-torque injects energy into the system. This energy injection is responsible for the emergence of self-sustained precessional motions [20]. The spin-transfer torque coefficient is [55,54,52,56] $g = \hbar J\,(2ed\mu_o M_s^2)^{-1} Pf\,(\mathbf{m}\cdot\hat{\mathbf{p}})$, where e is the electron charge, $\hbar$ the Planck constant, J is the current density and is of order 10^8 A/cm^2 [46], d the thickness of the layer and P describes the polarization at the interface between the ferromagnet and the spacer. For small applied currents, the magnetization dependence of the spin-transfer torque, $f\,(\mathbf{m}\cdot\hat{\mathbf{p}})$, can be assumed irrespective of $\mathbf{m}$ such that $f \approx 1$. This is known as the sine-approximation [54,55], and it is commonly adopted for certain types of nanopillars [55,52,56].

We focus on the self-organized dynamics that emerge as a consequence of the balance between two opposite effects: the current stabilizing the parallel state and the external field destabilizing it. Both the external magnetic field $\mathbf{h_a}$ and the polarization of the current $\hat{\mathbf{p}}$ point along the x-axis direction that allows the magnetization switching between the two equilibrium states, the parallel $\mathbf{m} = \mathbf{e_x}$ and the antiparallel state, $\mathbf{m} = -\mathbf{e_x}$.

Fig. 2 shows the bifurcation diagram of the system in the parameters space $\{g, h_a\}$, reproduced from Ref. [57], which is briefly described as follows. The parallel state is stable in the colored (light green) region. The horizontal (red) curve realizes stationary instability, while the dashed-dotted (green) thick diagonal line accounts for the Andronov-Hopf bifurcation [1–3], and it produces precessions for $g \geqslant \alpha(h_a + \beta_x + \beta_z/2)$. This behavior has been reported on a nanopillar, where the frequency is typical of the order of microwaves [8].

When considering the exchange energy *spatial instabilities* may appear [2]. In the system under study, this occurs for $g \geqslant g_c = -\beta_z/2$ which is represented by the vertical dashed blue line in Fig. 2. A negative value of g favors the parallel configuration due to the current transport and the magnetic moment of the fixed layer whereas a negative value of h_a destabilizes the parallel state. The spatial instability of the parallel state will occur when the current is not strong enough to

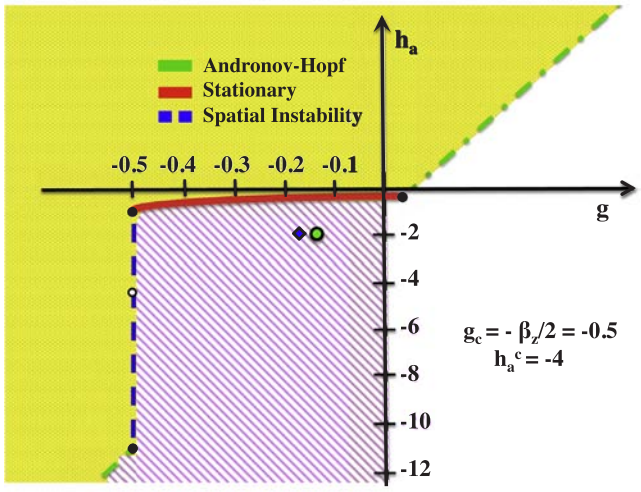

Fig. 2. Bifurcation diagram of the spin-valve described by Eq. (2) in the parameter space $\{g, h_a\}$. The parallel state is stable in the dotted (light green) region. The dashed-dotted (green) diagonal line accounts for the Andronov-Hopf bifurcation. The bold (red) curve realizes stationary instability. The vertical (blue) dashed line accounts for the spatial instability curve. The blue diamond and the green dot correspond to the states depicted in Fig. 3 and Fig. 5, respectively. The bifurcation diagram has been reproduced from Ref. [57]. (For interpretation of the references to colour in this figure legend, the reader is referred to the web version of this article.)

annul the effect of the external field, that is for $g \geqslant g_c = -\beta_z/2$. On the other hand, the instability condition for the antiparallel state is $g \leqslant \beta_z/2$ [58]. Two natural equilibria, the parallel $\mathbf{e_x}$ and antiparallel state $-\mathbf{e_x}$, are both extremes of the free energy E of the system and are related by the transformation $(g, h_a) \to (-g, -h_a)$. Therefore, due to the symmetries of Eq. (2) the antiparallel state of the free magnetization has an analogous phase diagram to the parallel state with the opposite sign of g and h_a.

For values of $g > g_c$, that is when one crosses the dashed vertical line, the appearance of spatial patterns arises due to the instability of the parallel state $\mathbf{m} = \mathbf{e_x}$. We will focus our study on the striped (purple) region characterized by a smaller magnetic field. In particular, we will study how an increase of our control parameter g, what is equivalent to diminish dissipation [57] or increase injection, will induce rich spatiotemporal dynamics in the system.

3. Simulations

Eq. (2) is numerically solved using a variable-step fifth-order Runge–Kutta (RK5) scheme for the temporal evolution [59]. The differential operators are approximated by centered schemes of sixth order. Space is discretized in $N = 501$ points using finite differences of stepsize $\Delta x = 0.054$, this corresponds to a length of $L = (N-1)\Delta x = 27$ in exchange length units. To study the extensive properties of the system and the robustness of the solutions, we have also performed several simulations for different values of N and Δx. We use Neumann boundary conditions, that is, $\partial_x \mathbf{m} = 0$ at $x = 0, L$. After any transients have faded away, we have continued the calculations for at least twice the full transient time with a maximum integration time 10^4.

The rest of this section is divided into two parts. At the first subsection, the quantities that are commonly used to describe complex regimes are introduced. At the second one, the numerical results are analyzed to identify the different type of dynamical behaviors.

3.1. Dynamical indicators

A simple physical quantity that globally characterizes the dynamics in time is the spatial average of the magnetization, given by:

$$\mathbf{m}^{av}(t) \equiv \frac{1}{L}\int_0^L \mathbf{m}(t, x)dx. \tag{3}$$

This indicator is used to study the temporal dynamics of the magnetization. As a consequence of its structure composed of alternating ferromagnetic and non-magnetic layers, spin valves exhibit a phenomenon called *Giant Magneto-Resistance* (GMR) [60,61,53,62]. This resistance accounts for the spin-dependent scattering, which renders devices with antiparallel magnetizations more resistive compared to other configurations. It is possible to produce a large change in resistance (can be as high as 200% [60]) of the multilayer in response to altering the relative magnetization orientation of the ferromagnetic layers, low when the magnetizations of neighboring ferromagnetic layers are parallel (r_P) and high when they are antiparallel (r_{AP}).

The electrical resistance r is a congruous indicator because it can be easily measured experimentally. The spatial average is usually approximated as [63]

$$R \equiv \frac{r(m_x^{av}) - r_P}{r_{AP} - r_P} \simeq \frac{1 - m_x^{av}}{2}. \tag{4}$$

A hallmark of chaotic dynamical behaviors is the exponential separation of the nearby trajectories in time. Lyapunov exponents describe the rate of exponential divergence from perturbed initial conditions [65,64] and serve as a useful tool to quantify chaos. The largest Lyapunov exponent ($\lambda_{\max}$) is defined as

$$\lambda_{\max} = \lim_{t\to\infty}\left[\frac{1}{t}\ln\left(\frac{\|\delta\mathbf{m}(t, x)\|}{\|\delta\mathbf{m}(t_0, x)\|}\right)\right], \tag{5}$$

where $\|\bullet\| \equiv (L^{-1}\int_0^L dx\, |\bullet|^2)^{1/2}$, t_0 is the initial time, and $\delta\mathbf{m}$ satisfies the partial differential equation:

$$\frac{\partial\delta\mathbf{m}}{\partial t} = \bar{\mathbf{J}}\cdot\delta\mathbf{m}, \tag{6}$$

where $\bar{\mathbf{J}}(\mathbf{m})$ is the Jacobian matrix of the system. In a continuous system, two magnetic configurations that were infinitesimally close at $t = 0$, separate in phase space exponentially fast when the system is chaotic, $\lambda_{\max} > 0$. On the other hand, for a negative largest Lyapunov exponent ($\lambda_{\max} < 0$), the two initially close states converge to the same equilibrium. The marginal case $\lambda_{\max} = 0$ corresponds to solutions where orbits are time-periodic, quasi-periodic, or non-chaotic saddle state. In the present case, we discretize the time and use magnetization trajectories separated by a distance $\|\delta\mathbf{m}(t_0, x)\| \sim 10^{-8}$. In order to avoid any transients we calculate $\lambda_{\max}$ from $t_0 = 2\times10^4$ up to $t_{max} = 3\times10^4$. With the purpose to overcome exponential divergences, we rescale $\|\delta\mathbf{m}(t, x)\|$ by the initial norm $\|\delta\mathbf{m}(t_0, x)\|$ every 100 iterations.

3.2. Results

Two simple solutions can be distinguished as it is shown in Fig. 3, the uniform antiparallel state, $m_x = -1$ (dashed line), and a chaotic pattern around the parallel state $m_x = 1$ (continuous line). For $h_a = -2$, the antiparallel uniform state is stable only for $g > -0.15$ [58,57]. Hence, the system presents coexistence between these two magnetic configurations. In the next subsubsections, we analyze the dynamical properties of these solutions and the spatial connections between them.

3.2.1. Patterns

The system presents chaotic and regular patterns as a function of the control parameters. The inset of Fig. 3 shows the spatiotemporal evolution of the component m_x for a chaotic pattern. The time evolution is up to 2000 iterations (time steps) displaying an aperiodic dynamic with positive $\lambda_{\max} = 0.1641$. The temporal average of the energy and the reduced magnetoresistance are $\langle E\rangle = 1.711$ and $\langle R\rangle = 0.159$, respectively. A small value of the resistance agrees with the hypothesis of low resistances for nearly parallel configuration in spin valves [66–68].

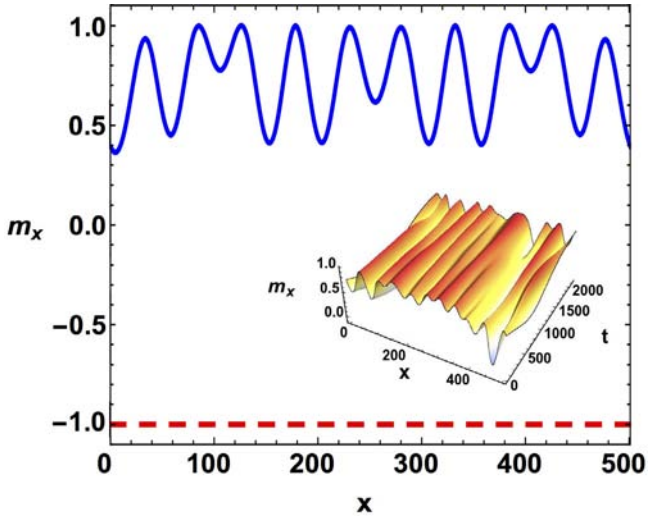

Fig. 3. Magnetization component m_x at $h_a = -2.0$ and $g = -0.18$. The light (red) dashed line corresponds to the uniform state $m_x = -1$ and the continuous (blue) curve corresponds to the chaotic pattern around $m_x = 1$. The inset shows the spatiotemporal diagram of m_x for the chaotic pattern around the parallel state. The value of $\lambda_{\max} = 0.164$, while temporal average of the energy and giant-magneto resistance are $\langle E \rangle = 1.711$ and $\langle R \rangle = 0.159$, respectively. (For interpretation of the references to colour in this figure legend, the reader is referred to the web version of this article.)

To study the extensive properties of the chaotic pattern, we have performed several simulations with different lengths, $L = (N-1)\cdot dx$, by varying the number of points N that compose the size of the box for a fixed value of the discretization step size dx. The Fig. 4 shows four different cases for $N = 101, 201, 301, 401$. The right upper insets correspond to the spatiotemporal profiles of the component m_x. It can be appreciated an aperiodic and more complex behavior as the size of the system is increased. The values of the largest Lyapunov exponent are displayed for each case, a positive value of λ_{max} denotes chaotic behavior. In addition, a continuum Fourier spectrum is observed, which is a common feature of chaotic states. Our results reveal that chaos is present for all the values of N considered here. Notice that the number of observed frequencies of the spectrum is increased with N, expected for extensive chaos.

On the other hand, since two solutions coexist, other families of states can be created. In the next subsections, we analyze the possibility of having different types of solutions that connect both magnetic configurations, *fronts* (or domain walls) and *localized structures*.

3.2.2. Fronts

Front solutions usually emerge in systems with bistability [2,21,25,69], that is, systems with two stable solutions. However, front states do not require bistability to exist. In the present context, the fronts are domain walls that separate regions where the magnetization has different orientations. In particular, fronts connect asymptotically a uniform state—the antiparallel equilibrium—with a spatiotemporal pattern around the parallel state. The upper panel of Fig. 5 shows a front state at fixed parameters $h_a = -2.0$ and $g = -0.14$. By varying the initial conditions, we can create different types of fronts or localized domains. The first configuration accounts for a solution that connects both extended states and the second is characterized by displaying a state surrounded by the other one.

In addition, the lower panel of Fig. 5 shows the largest Lyapunov exponent ($\lambda_{\max}$) with the same front initial condition. The simulations proceed by fixing the applied magnetic field h_a and sweeping the current density g in steps of $\Delta g = 0.01$. We observe regular behavior for g values close to $g_c \approx -\beta_z/2$ or $g \approx 0$. In the intermediate region, positive values of $\lambda_{\max}$ denote chaotic behavior. The chaotic region with positive $\lambda_{\max}$ is also increased as the strength of the applied field is increased. The reason for this fact is the amplitude growth of the pattern for higher values of h_a. Transitions among regular and chaotic states are visible when $\lambda_{\max}$ jumps abruptly from a negative or zero value to a positive

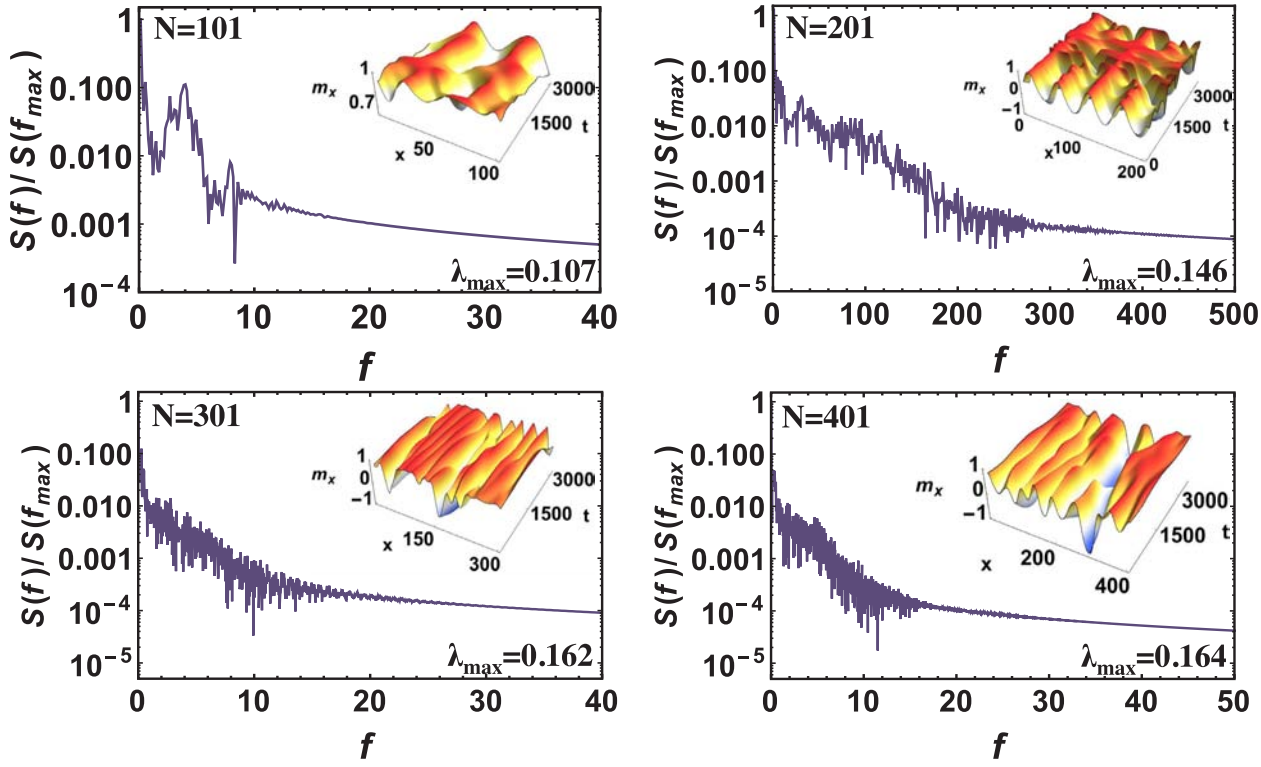

Fig. 4. Characterization of the chaotic pattern at $h_a = -2.0$ and $g = -0.18$. Fourier power spectrum $S(f)$ of m_x for different sizes of the simulation box N = 101, 201, 301, 401. The right upper insets correspond to the spatiotemporal profiles of the component m_x. The value of $\lambda_{\max}$ is showed for each case.

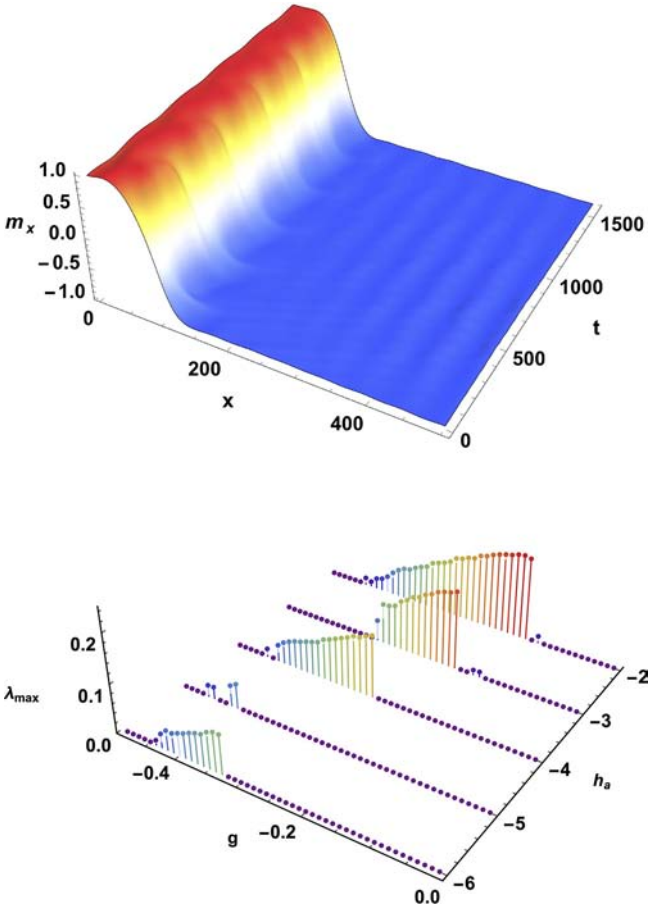

Fig. 5. (Up) Spatiotemporal dynamics of the component m_x at $h_a = -2.0$ and $g = -0.14$. Here, $\lambda_{\max} = 6.8{\cdot}10^{-3}$, $\langle E\rangle = -1.41$ and $\langle R\rangle = 0.815$. (Down) Largest Lyapunov exponent for a front initial condition as a function of h_a and g.

one. The error of $\lambda_{\max}$ is of order 10^{-4}.

3.2.3. Localized structures

Since we have observed front states, one expects the existence of localized structures, which are interpreted as a bounded state of two domain walls [25,33]. Notice that localized structures can be observed in a wide range of physical phenomena [34]. In the coexistence region, we can induce different localized structures by making a local perturbation of the extended magnetic configuration state. The developed localized structure will present a particular size and shape depending on the given initial condition, as it is observed in Fig. 6. On the left panel a valley initial condition is given with

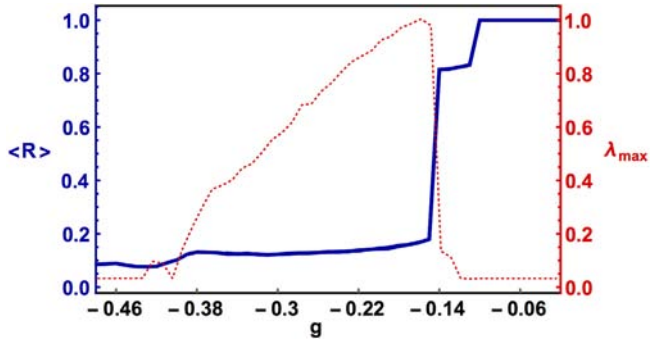

Fig. 7. Reduced magnetoresistance thick (blue) line, and largest Lyapunov exponent dashed (red) line, as a function of the current g at $h_a = -2.0$ with a hump initial condition. (For interpretation of the references to colour in this figure legend, the reader is referred to the web version of this article.)

$\lambda_{\max} = 0.106$, $\langle E\rangle_{valley} = -1.841$ and $\langle R\rangle_{valley} = 0.904$. The center and the right panels represent an initial hump condition given at different position of the box with $\langle E\rangle_{hump} = -1.409$ and $\langle R\rangle_{hump} = 0.815$. Here, $\lambda_{\max} = 0.018$ and $\lambda_{\max} = 0.016$, respectively. Notice that the localized states emit waves with different amplitude and wavenumber. The difference between the energy and the resistance values for the valley and the hump state can be useful when analyzing the experimental results.

Due to the GMR effect [60,61], the lowest resistance state corresponds to a magnetic parallel configuration because a portion of the current in which the spin is aligned with the magnetic layers shows little angle scattering [70]. On the other hand, the high resistance state is because no portion of the current may pass through the layer without significant scattering when the layers are antiparallel oriented. Eq. (4) implies that $R = 1$ for the antiparallel state and $R = 0$ for the parallel state. Therefore, the minimum of the reduced magnetoresistance is reached at $m_x = 1$, while the maximum is found at $m_x = -1$.

Fig. 7 shows the reduced magnetoresistance (blue line) and the largest Lyapunov exponent (red dashed line) at $h_a = -2.0$ as a function of g for localized states. At $g \approx -0.14$ the resistance undergoes an abrupt jump to a higher value and the magnetization suffers a transition between chaotic and regular dynamic. It is noteworthy that the localized structures with low resistance are chaotic, although the regular ones have a high resistance when the applied current is close to 0.

According to this result, in Fig. 8 we study the values of the applied current that produces switching of the magnetic layers between the low-resistance (parallel) and high-resistance (antiparallel) states for different values of h_a. The simulations reproduce abrupt changes as the current is increased following a linear law such as $\langle R\rangle_{change} = 0.79 g_{change} + 0.28$. The shifts fulfill the condition of instability for the antiparallel state $g \leqslant \alpha(h_a - \beta_x - \beta_z/2)$. For instance, at $h_a = -2.0$ the system increases the resistance at $g \approx -0.15$ while at $h_a = -5.0$ the change occurs at $g \approx -0.30$. The inset shows a linear law

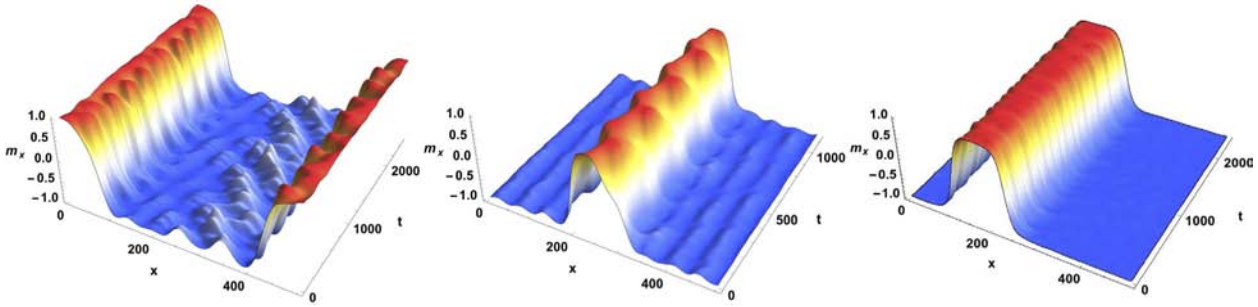

Fig. 6. Spatiotemporal dynamics of the component m_x for localized structures with different initial conditions at $h_a = -2.0$ and $g = -0.14$. On the left panel a valley initial condition is given, the center and right panels have a hump initial condition located in different positions of the box. Here $\lambda_{\max_1} = 0.106$ and $\lambda_{\max_2} = 0.018$, and $\lambda_{\max_3} = 0.016$, while $\langle E\rangle_1 = -1.841$, $\langle E\rangle_2 = -1.409$, $\langle E\rangle_3 = -1.409$, $\langle R\rangle_1 = 0.904$, $\langle R\rangle_2 = 0.815$ and $\langle R\rangle_3 = 0.815$ respectively. Notice that the localized states emit waves with different amplitudes and wavenumbers.

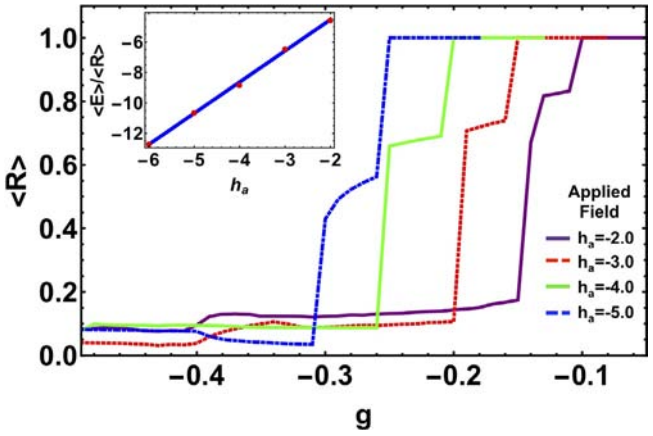

Fig. 8. Reduced magnetoresistance versus current g for different values of the applied magnetic field h_a. The inset shows a linear dependence $\langle E\rangle = (-2.053h_a - 0.418)\langle R\rangle$ with a front initial condition.

between the magnetic energy and the resistance $\langle E\rangle = (-2.053h_a - 0.418)\langle R\rangle$. The magnetic energy is not directly accessible, but voltage measurements are sufficient to calculate the resistance [67,68] and consequently the energy. This behavior remains valid for both, fronts and localized structures, hence it can be useful to identify the transitions among states experimentally.

Fig. 9 presents two bifurcation diagrams as a function of the current at a fixed applied field $h_a = -4.5$. Firstly, we calculate the temporal series of the magnetic energy and the reduced magnetoresistance and after we record the values of g every time a local maximum is reached. To distinguish between regular and chaotic states, we compute the largest Lyapunov exponent. The (gray) shaded area, between $g = (-0.43, -0.33)$, stands for the chaotic behavior of the system where the largest Lyapunov exponent is positive. Indeed, the transition from regular to chaotic dynamics is demonstrated. Notice that the chaotic behavior disappears by means of the so-called *crisis* mechanism at $g = -0.33$. A crisis is defined as the collision between a chaotic attractor with a periodic orbit or an unstable fixed point [71,2]. For periodic solutions, the magnetization follows a unique trajectory, that is, a single maximum is reached. The appearance of regions compounded by multiples points indicates coexistence of states with different dynamical behavior. The first bifurcation at $g = -0.47$ [enlarged in the upper right inset of Fig. 9.a)] is a signature of the coexistence between states with period doubling. Nevertheless, for $-0.247 \leqslant g \leqslant -0.235$, some multiple-period states also appear. A significant jump at $g = -0.29$ indicates a change in the type of regular states. As we increase g (beyond $g = -0.23$), the system suffers a reduction of the periodicity with no significant changes in the values of the energy and the resistance.

For a more in-depth insight, we study two particular cases. The spatiotemporal profiles of m_x for a chaotic and a regular state are represented in the left and right insets at the bottom of Fig. 9.a), respectively. The middle and the lower parts of Fig. 9 show a parametric plot of the spatial averages of the magnetization m_x^{av} and m_y^{av} and the corresponding Fourier power spectra of m_x^{av}. The red dot at $g = -0.40$ corresponds to the chaotic state with $\lambda_{\max} = 0.029 \pm 0.001$. Two characteristic signs reflect the chaotic dynamic: the parametric plot showed as a sharp curve in panel b) and the broadly distributed Fourier spectrum of panel c). The red triangle at $g = -0.25$ indicates the regular case with $\lambda_{\max} = (7.08 \pm 0.62)\cdot 10^{-5}$. The closed curve illustrates the regular behavior at panel d) and the well-defined peaks of the Fourier spectrum at panel e) related to five different predominant frequencies.

4. Final remarks

In summary, we have shown that spin valves that combine the effects of the spin-polarized current, the spatial coupling and the dissipation allow the emergence of chaotic textures. We characterized the observed dynamic quantitatively using the largest Lyapunov exponent. The coexistence region is characterized by spatial domains with interfaces that connect asymptotically a non-trivial uniform state with a spatiotemporal pattern, the front solutions. As a consequence of the dynamical behavior of the pattern, we found that localized structures can be regular or chaotic. We characterize these states with the largest Lyapunov exponent, bifurcation diagrams, parametric plots and the Fourier spectrum for the spatial average of the magnetization. These indicators show multiple transitions between chaotic and regular states. In fact, the chaotic pattern showed in Fig. 3 exhibits chaos for different device sizes as it is shown in the Fig. 4.

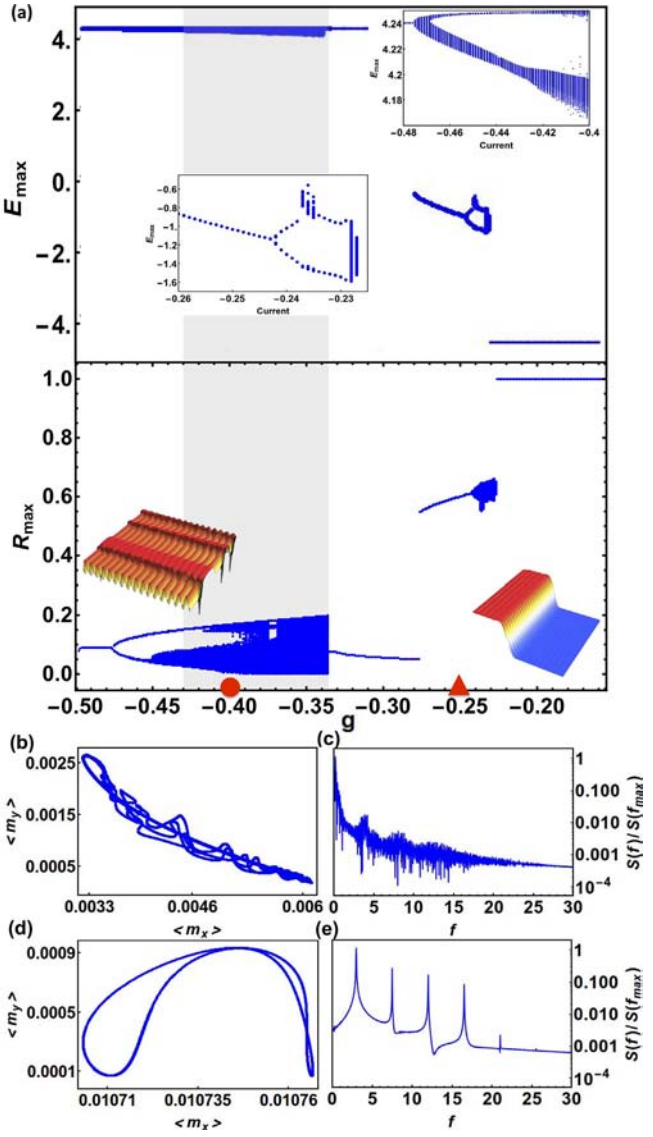

Fig. 9. a) Bifurcation diagram of the magnetic energy and the reduced magnetoresistance maxima E_{max} and R_{max} with a hump initial condition at $h_a = -4.5$ as a function of g. The (grey) shaded region indicate chaotic behavior ($\lambda_{\max} > 0$). Frames b) and d) are the parametric plot of m_x^{av} and m_y^{av} and c) and e) are the corresponding Fourier power spectra of $m_x^{av}$for a chaotic case (red dot) at $g = -0.40$ and a regular case (red triangle) at $g = -0.25$ displayed in the left and right insets respectively. The amplitudes of the power spectra are normalized and expressed in arbitrary units. (For interpretation of the references to colour in this figure legend, the reader is referred to the web version of this article.)

Finally, let us present the phase diagram of the system, displayed in Fig. 10. The vertical black line corresponds to the limit of the critical

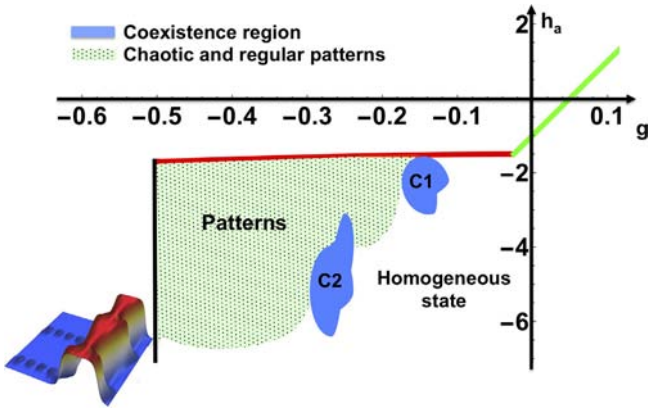

Fig. 10. Phase diagram of Eq. (2). The shaded (blue) zones indicate the coexistence region of patterns, fronts and localized structures. Chaotic and regular patterns emerge in the green dotted area. The uniform state is found in the homogeneous region. The left inset displays a complex time-dependent soliton at $h_a = -2.0$ and $g = -0.125$ placed at C1. (For interpretation of the references to colour in this figure legend, the reader is referred to the web version of this article.)

current $g_c = -0.5$ and delimits the appearance of stationary patterns. For small values of h_a near g_c the patterns are regular, but as we increase $|h_a|$, the pattern amplitude grows, and the texture becomes chaotic. The regions marked as C1 and C2 correspond to the areas of coexistence among patterns, fronts, and localized and homogeneous states characterized in Figs. 3, 5, 6 and 9, being fronts the most likely particle states. Inside C1 we find a rich variety of structures of different sizes and shapes. The inset displays a particular soliton state, namely a *breather* soliton [32,37], found at $h_a = -2$ and $g = -0.125$. A complex time-dependent behavior characterizes this state because both the amplitude and the width can vary in space and/or time. This internal motion can be periodic, quasi-periodic or chaotic, in our case the breather has a periodic motion. Within the region C2 we find front, pattern, and valleys solutions. Chaotic and regular patterns appear in the green dotted region. As we approximate to $g = 0$ the uniform state around $m_x = -1$ becomes stable with no positive $\lambda_{\max}$. This variation is also reflected in the left panel of Fig. 5. Moreover, according to Fig. 7 at $h_a = -2.0$ the regular states for $g > -0.14$ have a higher value of the resistance due to an antiparallel homogeneous solution, same as the states at $h_a = -4.5$ for $g > -0.27$. We confirm the relationship between the condition of instability for the antiparallel state $g \leqslant \alpha(h_a - \beta_x - \beta_z/2)$ and the values of g where the states suffer an abruptly increase of the resistance. Hence, the structures with low resistance are chaotic while the high resistance structures have regular behavior.

From Fig. 10, we conclude that the variation of the control parameters h_a and g can induce primary and secondary bifurcations to the system. We determine two relevant zones of coexistence regions in which we find patterns, fronts and localized states. Experimentally, one can identify chaotic dynamic generated by the deterministic perturbation. For example, when g is increased at a fixed value of h_a, the current-driven power spectrum should turn into nonchaotic dynamics to chaos and back to regular regimes. Since thermal fluctuations are inevitable for room-temperature applications, we have also studied the stability of the solutions as a function of the temperature. In particular, we found that the localized states are stable in wide a range of temperature.

Acknowledgments

AMC and DL acknowledge partial financial support from FONDECYT 1180905 and Centers of excellence with BASAL/CONICYT financing, Grant FB0807, CEDENNA. MGC thanks for the financial support of Millennium Institute for Research in Optics and FONDECYT project 1180903.

Appendix A. Supplementary data

Supplementary data associated with this article can be found, in the online version, at https://doi.org/10.1016/j.jmmm.2019.01.027.

References

[1] G. Nicolis, I. Prigogine, Self-Organization in Nonequilibrium Systems, J. Wiley and Sons, New York, 1977.
[2] M.C. Cross, P.C. Hohenberg, Rev. Mod. Phys. 65 (1993) 851.
[3] R. Hoyle, Pattern Formation: An Introduction to Methods, Cambridge University Press, Cambridge, 2005.
[4] K. Nozaki, N. Bekki, Phys. D 21 (1993) 381.
[5] D. Ruelle, F. Takens, Commun. Math. Phys 20 (1971) 167.
[6] K. Kankeo, Phys. D 34 (1989) 1.
[7] G. Nicolis, Introduction to Nonlinear Science, Cambridge University Press, Cambridge, 1995.
[8] S.I. Kiselev, J.C. Sankey, I.N. Krivorotov, N.C. Emley, R.J. Schoelkopf, R.A. Buhrman, D.C. Ralph, Nature 425 (2003) 380–383.
[9] W.H. Rippard, M.R. Pufall, S. Kaka, S.E. Russek, T.J. Silva, Phys. Rev. Lett. 92 (2004) 027201.
[10] V.E. Demidov, S. Urazhdin, G. de Loubens, O. Kleind, V. Cros, A. Anane, S.O. Demokritov, Phys. Rep. 673 (2017) 1.
[11] D.V. Vagin, O.P. Polyakov, J. Magn. Magn. Mater. 320 (2008) 3394–3399.
[12] F. Matsukura, Y. Tokura, H. Ohno, Nat. Nano 10 (2015) 209.
[13] B. Heinrich, Y. Tserkovnyak, G. Woltersdorf, A. Brataas, R. Urban, G.E.W. Bauer, Phys. Rev. Lett. 90 (2003) 187601.
[14] J.C. Slonczewski, J. Magn. Magn. Mater. 150 (1995) 13–24.
[15] J.C. Slonczewski, J. Magn. Magn. Mater. 159 (1996) L1.
[16] L. Berger, Phys. Rev. B 54 (1996) 9353.
[17] Z. Li, S. Zhang, Phys. Rev. B 68 (2003) 024404.
[18] G. Bertotti, C. Serpico, I.D. Mayergoyz, A. Magni, M. d' Aquino, R. Bonin, Phys. Rev. Lett. 94 (2005) 127206.
[19] D.C. Ralph, M.D. Stiles, J. Magn. Magn. Mater. 320 (2008) 1190–1216.
[20] M. Lakshmanan, Philos. Trans. R. Soc. A 369 (2011) 1280.
[21] L.M. Pismen, Patterns and Interfaces in Dissipative Dynamics, Springer, 2006.
[22] M.G. Clerc, S. Coulibaly, D. Laroze, Phys. Rev. E 77 (2008) 056209.
[23] M.G. Clerc, S. Coulibaly, D. Laroze, Int. J. Bifurcation Chaos 19 (2009) 3525.
[24] P.E. Wigen, Nonlinear Phenomena and Chaos in Magnetic Materials, World Scientific, Singapore, 1994.
[25] P. Coullet, Int. J. Bifurcation Chaos 12 (2002) 2445.
[26] A.M. Kosevich, B.A. Ivanov, A.S. Kovalev, Phys. Rep. 194 (1990) 117.
[27] A. Slavin, V. Tiberkevich, Phys. Rev. Lett. 95 (2005) 237201.
[28] S. Bonetti, V. Tiberkevich, G. Consolo, G. Finocchio, P. Muduli, F. Mancoff, A. Slavin, J.A. Kerman, Phys. Rev. Lett. 105 (2010) 217204.
[29] R.K. Dumas, E. Iacocca, S. Bonetti, S.R. Sani, S.M. Mohseni, A. Eklund, J. Persson, O. Heinonen, J.A. Kerman, Phys. Rev. Lett. 110 (2013) 257202.
[30] J.M. Soto-Crespo, M. Grapinet, P. Grelu, N. Akhmediev, Phys. Rev. E 70 (2004) 066612.
[31] D. Urzagasti, D. Laroze, M.G. Clerc, H. Pleiner, Europhys. Lett. 104 (2013) 40001.
[32] M. Bondilla, I.V. Barashenkov, M.M. Bogdan, Phys. D 87 (1995) 314.
[33] R. Hertel, W. Wulfhekel, J. Kirschner, Phys. Rev. Lett. 93 (2004) 257202.
[34] O. Thual, S. Fauve, J. Phys. France 49 (1988) 303001.
[35] P. Coullet, C. Riera, C. Tresser, Phys. Rev. Lett 84 (2000) 3069.
[36] A. Ankiewics, N. Akhmediev, Dissipative Solitons: From Optics to Biology and Medicine, Springer, Berlin, 2008.
[37] R.J. Deissler, H.R. Brand, Phys. Rev. Lett. 74 (1995) 4847.
[38] A.O. Leon, D. Laroze, M.G. Clerc, A.M. Cabanas, Commun. Nonlinear Sci. Numer. Simul. 44 (2017) 404.
[39] Z. Yang, S. Zhang, Y.C. Li, Phys. Rev. Lett. 99 (2007) 134101.
[40] Y. Lan, Y.C. Li, Nonlinearity 21 (2008) 2801.
[41] S. Murugesh, M. Lakshmanan, Chaos 19 (2009) 043111.
[42] P.P. Horley, M.Y. Kushnir, M. Morales-Meza, A. Sukhov, V. Rusyn, Phys. B 486 (2016) 60.
[43] X. Zhu, J.-G. Zhu, R.M. White, J. Appl. Phys. 95 (2004) 6630.
[44] D. Berkov, N. Gorn, Phys. Rev. B 71 (2005) 052403.
[45] A.M. Cabanas, L.M. Pérez, D. Laroze, J. Magn. Magn. Mater. 460 (2018) 320–326.
[46] D. Mayergoyz, G. Bertotti, C. Serpico, Nonlinear Magnetization Dynamics in Nanosystems, Elsevier, North Holland, 2009 and references therein.
[47] J. Brandenburg, R. Hühne, L. Schultz, V. Neu, Phys. Rev. B 79 (2009) 054429.
[48] M.T. Johnson, P.J.H. Bloemen, F.J.A. den Broeder, J.J. de Vries, Rep. Prog. Phys. 59 (1996) 1409.
[49] B. Dieny, M. Chshiev, Rev. Mod. Phys. 89 (2017) 025008.
[50] W. Brown, Micromagnetics, Wiley, New York, 1963.
[51] T.L. Gilbert, IEEE Trans. Magn. 40 (2004) 3443.
[52] S.-W. Lee, K.J. Lee, IEEE Trans. Magn. 46 (2010) 2349.
[53] K.-J. Lee, A. Deac, O. Redon, J.-P. Nozières, B. Dieny, Nat. Mater. 3 (61) (2004) 877.
[54] D.V. Berkov, J. Miltat, J. Magn. Magn. Mater. 320 (2008) 1238.
[55] J. Xiao, A. Zangwill, Phys. Rev. B 72 (2005) 014446.
[56] W. Kim, S.W. Lee, K. Lee, J. Phys. D: Appl. Phys. 44 (2011) 384001.
[57] A.O. Leon, M.G. Clerc, S. Coulibaly, Phys. Rev. E 89 (2014) 022908.

[58] M.G. Clerc, S. Coulibaly, D. Laroze, A.O. Leon, A. Nuñez, Phys. Rev. B 91 (2015) 224426.
[59] W.H. Press, S.A. Teukolsky, W.T. Vetterling, B.P. Flannery, Numerical Recipes in C: The Art of Scientific Computing, Cambridge University Press, New York, 1992.
[60] M.N. Baibich, J.M. Broto, A. Fert, F.N.V. Dau, F. Petroff, P. Eitenne, G. Creuzet, A. Friederich, J. Chazelas, Phys. Rev. Lett. 61 (1988) 2472.
[61] M.G. Binasch, P. Grünberg, F. Saurenbach, W. Zinn, Phys. Rev. B 39 (1989) 4828.
[62] K. Tarawneh, N. Al-Aqtash, R. Sabirianov, J. Magn. Magn. Mater. 363 (2014) 44–48.
[63] W.P. Pratt Jr., S.-F. Lee, J.M. Slaughter, R. Loloee, P.A. Schroeder, J. Bass. Phys. Rev. Lett. 66 (1991) 3060.
[64] A. Wolf, J.B. Swift, H.L. Swinney, J.A. Vastano, Phys. D 16 (1985) 285.
[65] A. Pikovsky, A. Politi, Lyapunov Exponents: A Tool to Explore Complex Dynamics, Cambridge University Press, Cambridge, 2016.
[66] J.A. Katine, F.J. Albert, R.A. Buhrman, E.B. Myers, D.C. Ralph, Phys. Rev. Lett. 84 (2000) 3149.
[67] J. Bass, W.P. Pratt Jr., J. Magn. Magn. Mater. 200 (1999) 274.
[68] S. Zhang, P.M. Levy, A. Fert, Phys. Rev. Lett. 65 (1990) 13.
[69] M. Leconte, J. Martin, N. Rakotomalala, D. Salin, Phys. Rev. Lett. 90 (2003) 128302.
[70] J.W. Lau, J.M. Shaw, J. Phys. D: Appl. Phys. 44 (2011) 303001.
[71] C. Grebogi, E. Ott, J.A. Yorke, Phys. D 7 (1983) 181.